

ORIGINAL ARTICLE

Pencil-Code special edition: modelling supernova driven turbulence

F. A. Gent^{†*}, M-M. Mac Low^{††}, M. J. Käpylä^{◊†}, G. R. Sarson[‡] and J. F. Hollins[‡]

[†] ReSoLVE Centre of Excellence, Dept. Computer Science, Aalto University, FI-00076, Finland

^{††} Dept. Astrophysics, American Museum of Natural History, New York, 10024-5192, USA

[◊]Max Planck Institute for Solar System Research, 37707, Göttingen, Germany

[‡]School of Mathematics, Statistics and Physics, Newcastle University, Newcastle upon Tyne, NE1
 7RU, UK

(submitted May 2018)

High Mach number shocks are ubiquitous in interstellar turbulence. The Pencil Code is particularly well suited to the study of magnetohydrodynamics in weakly compressible turbulence and the numerical investigation of dynamos because of its high-order advection and time evolution algorithms. However, the high-order algorithms and lack of Riemann solver to follow shocks make it less well suited to handling high Mach number shocks, such as those produced by supernovae (SNe). Here, we outline methods required to enable the code to efficiently and accurately model SNe, using parameters that allow stable simulation of SN-driven turbulence, in order to construct a physically realistic galactic dynamo model. These include the resolution of shocks with artificial viscosity, thermal conductivity, and mass diffusion; the correction of the mass diffusion terms; and generalization of the Courant condition to include all source terms in the momentum and energy equations. We test our methods with the numerical solution of the 1D Riemann shock tube (Sod 1978), also extended to a 1D adiabatic shock with parameters and Mach number relevant to SN shock evolution, including shocks with radiative losses. We extend our test with the 3D numerical simulation of individual SN remnant evolution for a range of ambient gas densities typical of the interstellar medium and relate these to the analytical solutions of Sedov-Taylor (adiabatic) and the snowplough and Cioffi *et al.* (1988) results incorporating cooling and heating processes.

Keywords: Numerical methods; High Mach number shocks; Artificial diffusivity; Supernova driven turbulence; Instabilities

1. Introduction

Astrophysical turbulence often occurs in highly compressible flows (Elmegreen and Scalo 2004, Scalo and Elmegreen 2004). The Pencil Code¹ (Brandenburg and Dobler 2002) has been extensively applied to weakly compressible flows, such as occur in stellar turbulence (Haugen *et al.* 2004a), stellar magnetoconvection (Käpylä *et al.* 2008, 2009, 2012, 2016), stellar and planetary dynamos (Dobler *et al.* 2006, McMillan and Sarson 2005), and accretion disks (de Val-Borro *et al.* 2006, Käpylä and Korpi 2011). One of the more highly compressible environments is the interstellar medium (ISM), where turbulence is driven by repeated supernova (SN) explosions. The Pencil Code is well suited to the investigation of dynamos, both small scale (fluctuation or random) modes and large scale (mean or system-wide) modes. It uses sixth-order in space and third-order in time advection algorithms to capture the flow with near-spectral accuracy, and is optimized for excellent performance on clusters of superscalar processors.

*Corresponding author. Email: frederick.gent@aalto.fi

¹<https://github.com/pencil-code>

This code has been applied to the study of SN driven ISM turbulence and the galactic dynamo (Gent *et al.* 2013a,b, Käpylä *et al.* 2018). From these results a large scale dynamo (LSD) was obtained for a system resembling the solar neighbourhood of the Milky Way, but the parameters chosen resulted in magnetic Prandtl numbers varying strongly by phase, due to which a small-scale dynamo (SSD) was only present in the hot phase. Here we shall report on the improvements to the Pencil Code model — which include using only the minimum artificial viscosity needed to permit the resolution of strong shocks with Mach numbers of order 100, improvement of the mass diffusion algorithm, and force-dependent time constraints to improve the stability of the code — and test the results for various shocks.

Spectral methods are very effective for accurately solving initial value problems without discontinuities and well suited for elliptic equations. By reframing the problem as a superposition of basis equations they can be computationally intensive. Handling shocks would generally require handling this aspect of the calculation in the real space, applying similar tools as finite difference and volume element schemes. In this space artificial diffusion is normally required. Regardless of the order of accuracy of the various codes, artificial viscosity effectively reduces to a first order method in the vicinity of the shock. An alternative is to use Godunov methods to solve for the fluxes at zone boundaries. These rely on exact or approximate solutions to the Riemann problem at each zone boundary. Although accurate, they are computationally expensive and sensitive to the addition of new physics that can change the signal propagation characteristics.

In this article we shall explain the methods and parameter choices required for the Pencil Code to handle the 1D Riemann shock tube test (Section 2) and report its performance for various levels of shock reaching above Mach 100 (see Section 3). In Section 2.4, we describe some additions to the Pencil Code timestepping control, to maintain numerical stability for these challenging simulations. We shall then describe some additional steps required to handle highly compressible SN driven turbulence, including radiative cooling, and in Section 4 present the results of Sedov-Taylor and snowplough tests for SN remnant evolution across a range of ambient gas density and model resolution. Finally, we summarise our work in Section 5.

2. Method

Our strategy to model strong shocks is to use upwind differencing (effectively a form of hyperdiffusion) when solving each partial differential equation (PDE), to ensure the system is resolved at the grid scale; and to apply artificial viscosity and thermal diffusivity at the shock fronts, following Stone and Norman (1992), to avoid discontinuities in the derivatives by smoothing the shock profile. The current implementation of artificial diffusivities is adapted from the earlier treatments of Haugen *et al.* (2004b) and Mee (2007).

2.1. Artificial shock viscosity

In the momentum equation the shock capturing viscosity is applied as

$$\rho \frac{D\mathbf{u}}{Dt} = \dots + \nabla (\rho \zeta_\nu \nabla \cdot \mathbf{u}), \quad (1)$$

where \mathbf{u} denotes velocity, ρ gas density and

$$\frac{D}{Dt} = \frac{\partial}{\partial t} + \mathbf{u} \cdot \nabla$$

is the material derivative. The viscous coefficient takes the form

$$\zeta_\nu = \begin{cases} -\nu_{\text{shock}} \nabla \cdot \mathbf{u}, & \text{if } \nabla \cdot \mathbf{u} < 0, \\ 0, & \text{otherwise,} \end{cases}$$

with constant $\nu_{\text{shock}} \simeq 1$. Hence, the artificial viscosity is applied only locally at the shocks, and has quadratic dependence on the divergence. An additional source term in the equation of energy arises from the viscous heating produced by the artificial viscosity. We solve the energy equation in the form of the specific entropy s , so we have

$$\rho T \frac{Ds}{Dt} = \dots + \rho \zeta_\nu (\nabla \cdot \mathbf{u})^2, \quad (2)$$

where T denotes temperature.

In the Pencil Code, the value of the convergence of the flow is calculated at each point and then the maximum value applying at any immediately neighbouring point is adopted for the local value of ζ_ν . In the case of the SN forced turbulence we have found this adequate, but the sixth order scheme can permit adopting the maximal value up to a distance of three points. This offers greater stability at the expense of a more diffusive regime. The field ζ_ν is then smoothed using a simple seven-point smoothing polynomial (with weights [1, 6, 15, 20, 15, 6, 1]/64), and applied to Equations (1), (2).

2.2. Thermal Diffusion

Including a similar artificial thermal diffusion ζ_χ to the energy equation significantly damps numerical oscillations arising behind the shock front with negligible effect on the overall structure of the shock solutions. This takes the form

$$\rho T \frac{Ds}{Dt} = \dots + \nabla \cdot (c_p \rho \zeta_\chi \nabla T), \quad (3)$$

where c_p denotes the gas specific heat at constant pressure and the thermal diffusivity coefficient takes the form

$$\zeta_\chi = \begin{cases} -\chi_{\text{shock}} \nabla \cdot \mathbf{u}, & \text{if } \nabla \cdot \mathbf{u} < 0, \\ 0, & \text{otherwise.} \end{cases}$$

This coefficient is calculated using local maximums and smoothing, as for the artificial viscosity, above. A modest value $\chi_{\text{shock}} = 0.5$ is adequate for weak to moderate adiabatic shocks.

2.3. Mass diffusion

Finally, we consider the inclusion of mass diffusion. Mass diffusion is not necessary to model even strong shock solutions with the Pencil Code (as considered in detail in Section 3), although its use does tend to damp the oscillations in the wake of the shock. However, experiments with SN-driven turbulence show that shocks in that context are prone to local numerical instabilities where the density drops and the temperature rises without limit, producing a hot zone. The application of mass diffusion suppresses this problem.

With mass diffusion, in the absence of sinks or sources, the continuity equation becomes

$$\frac{D\rho}{Dt} = -\rho \nabla \cdot \mathbf{u} + \zeta_D \nabla^2 \rho + \nabla \zeta_D \cdot \nabla \rho, \quad (4)$$

where

$$\zeta_D = \begin{cases} -D_{\text{shock}} \nabla \cdot \mathbf{u}, & \text{if } \nabla \cdot \mathbf{u} < 0, \\ 0, & \text{otherwise.} \end{cases} \quad (5)$$

Adding a non-physical diffusion to the equation has consequences for the evolution of momentum and energy. This requires corrections to each equation to conserve momentum and energy. If we consider the momentum and energy equations absent the artificial diffusion, we have

$$\begin{aligned} \rho \frac{D\mathbf{u}}{Dt} &= \text{RHS}, & \rho \frac{De}{Dt} &= \text{RHS}, \\ \frac{D}{Dt}(\rho\mathbf{u}) - \mathbf{u} \frac{D\rho}{Dt} &= \text{RHS}, & \frac{D}{Dt}(\rho e) - e \frac{D\rho}{Dt} &= \text{RHS}, \\ \frac{D}{Dt}(\rho\mathbf{u}) + \mathbf{u}\rho \nabla \cdot \mathbf{u} &= \text{RHS}, & \frac{D}{Dt}(\rho e) + c_v T \rho \nabla \cdot \mathbf{u} &= \text{RHS}, \end{aligned}$$

where $e = c_v T$ denotes the internal energy and c_v is the specific heat at constant volume. When we include the mass diffusion in the continuity equation we obtain

$$\begin{aligned} \frac{D}{Dt}(\rho\mathbf{u}) + \mathbf{u} (\rho \nabla \cdot \mathbf{u} - \zeta_D \nabla^2 \rho - \nabla \zeta_D \cdot \nabla \rho) &\neq \text{RHS} \\ \frac{D}{Dt}(\rho e) + c_v T (\rho \nabla \cdot \mathbf{u} - \zeta_D \nabla^2 \rho - \nabla \zeta_D \cdot \nabla \rho) &\neq \text{RHS}. \end{aligned}$$

Hence, to conserve the properties of momentum and energy we must also deduct these extra terms from the respective RHS. For momentum we have

$$\rho \frac{D\mathbf{u}}{Dt} = \dots - \mathbf{u} (\zeta_D \nabla^2 \rho + \nabla \zeta_D \cdot \nabla \rho) \quad (6)$$

and for energy we have

$$\rho T \frac{Ds}{Dt} = \dots - c_v T (\zeta_D \nabla^2 \rho + \nabla \zeta_D \cdot \nabla \rho). \quad (7)$$

2.4. Timestep determination

The Pencil Code uses an explicit finite difference scheme, which can be faster than implicit schemes, but is not unconditionally stable. A necessary, although not necessarily sufficient, condition is to satisfy various Courant conditions on the time step, such as for advection and diffusion. For advection, this condition reads

$$\frac{1}{\delta t} \geq \max \left(\frac{U_{\max}}{c_{\delta t} \delta x_{\min}} \right), \quad (8)$$

where $c_{\delta t} < 1$ is the Courant number dedicated to the control of the advective timestep, and for the MHD case

$$U_{\max} = \max \left(|\mathbf{u}| + \sqrt{c_s^2 + v_A^2} \right).$$

c_s and v_A denote the sound speed and Alfvén speed, respectively. With maximal speeds of order 10^3 km s^{-1} typical of such turbulence, however, this is rarely significant in determining the maximum timestep. We also must account for the artificial diffusion terms we have introduced

to resolve shocks. The diffusive time step is controlled by the Courant condition

$$\frac{1}{\delta t} \geq \max \left(\frac{\zeta_{\max}}{c_{\delta t, v} \delta x_{\min}^2} \right), \quad (9)$$

where $c_{\delta t, v} < 1$ is a Courant coefficient for the diffusive timestep, $\zeta_{\max} = \max(\zeta_{\nu}, \gamma \zeta_{\chi}, \zeta_D)$ is the maximum diffusive coefficient acting at each point in the grid, and $\delta x_{\min} = \min(\delta x, \delta y, \delta z)$ the minimum grid spacing at each location. In the MHD case magnetic diffusivity ζ_{η} may also be included in ζ_{\max} .

It has previously been observed that strong heat sources or sinks can cause stresses on the numerical solvers that conventional timestep control described above does not address. In the context of ISM simulations and SN driven turbulence the effect of cooling and heating can cause numerical instability if not handled directly. Minimum cooling times are typically around 100 yr for the temperature and density ranges commonly considered in ISM simulations, but can be as low as 10 yr. This is not usually a problem as other processes often require shorter time resolution. Heating by SN is instant and therefore presents a challenge primarily through heat diffusion timescales. The main source of heating driving the timestep due to the supersonic flows is viscous heating. To ensure the heating/cooling time is resolved, the net heating H is summed and the timestep, δt constrained by its absolute maximum throughout the grid as

$$\frac{1}{\delta t} \geq \max \left(\frac{|H|_{\max}}{c_{\delta t, s} e} \right), \quad (10)$$

where $c_{\delta t, s} < 1$ controls the fractional change of energy permitted in any cell.

In weakly compressible flows the largest values on the right hand side of the entropy equation can be adequately resolved in time, but for the highly compressible flows of SN driven turbulence the sum of all changes to the energy can be many orders of magnitude greater than the evolving entropy of order unity. To address this the H_{\max} in Equation (10) is instead replaced by the maximal sum of the right hand side of the entropy equation $df(s)$, so that

$$\frac{1}{\delta t} \geq \max \left(\frac{|df(s)|_{\max}}{c_{\delta t, s} c_v} \right) \quad (11)$$

is used to constrain the timestep, with the maximum fractional change in entropy given by $c_{\delta t, s}$. We find empirically that this time step limit dominates immediately after SN explosions during SN driven turbulent runs.

The momentum equation must also be considered as a whole, similar to the treatment of the energy equation in Equation (9). The troublesome contribution to the code stability is to be found in viscous force, in general expressed as

$$\frac{D\vec{u}}{Dt} = \dots \nu \nabla^2 \vec{u} + \frac{\nu}{3} \vec{\nabla} \vec{\nabla} \cdot \vec{u} + 2\mathbf{S} \cdot \left(\nu \vec{\nabla} \ln \rho + \vec{\nabla} \nu \right) + \zeta_{\nu} \left(\vec{\nabla} \vec{\nabla} \cdot \vec{u} \right) + \vec{\nabla} \zeta_{\nu} \vec{\nabla} \cdot \vec{u},$$

involving the rate of strain tensor \mathbf{S} of the form

$$2S_{ij} = \frac{\partial u_i}{\partial x_j} + \frac{\partial u_j}{\partial x_i} - \frac{2}{3} \delta_{ij} \vec{\nabla} \cdot \vec{u}.$$

Note also, the viscous heat applying to the energy equation is proportional to $\mathbf{S}^2 \equiv S_{ij} S_{ij}$. In the diffusive timestep only the coefficients ν and ζ_{ν} are considered. The gradients in the expression are ignored, and in the case of SN turbulence, these contributions can be order $\pm 10^7$ – 10^9 . Increasing viscosity to smooth the gradients can be counter productive, making the viscous forces even larger. Instead, we limit the total change in momentum $df(\mathbf{u})$ with a

time step limitation of

$$\frac{1}{\delta t} \geq \max \left(\frac{|df(\mathbf{u})|_{\max}}{c_{\delta t,f} |\mathbf{u}|_{\text{nom}}} \right), \quad (12)$$

where $c_{\delta t,f} < 1$ is a Courant number applying to control of the forcing timestep, and $|\mathbf{u}|_{\text{nom}}$ is a sufficiently small nominal velocity. In practice $c_{\delta t,f} |\mathbf{u}|_{\text{nom}} \simeq 20$ is stable. An alternative approach might be to reduce $c_{\delta t,s} \ll 1$, but this would reduce the the timestep under all circumstances, whereas the forcing timestep control is more flexible and limits the timestep only when needed.

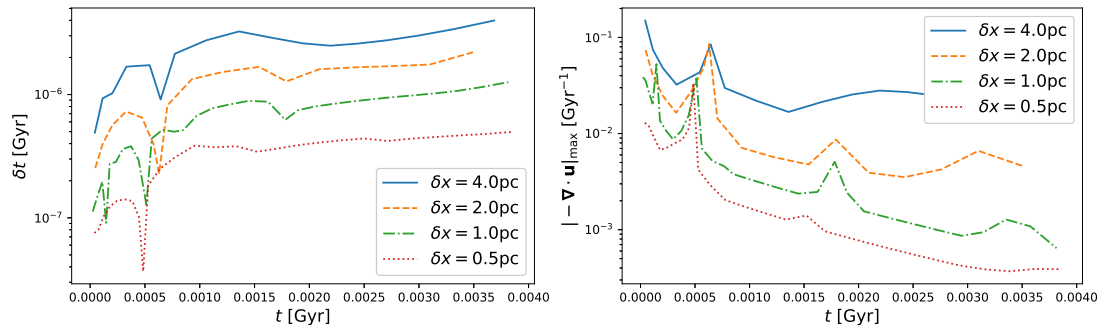


Figure 1. First panel: timestep evolution in unit ambient density single SN explosion runs with grid resolution of 4, 2, 1 and 0.5 pc. Second panel: evolution of the maximal value of convergence included in the artificial diffusion coefficients.

The timestep for snowplough tests (see Section 4.3) with grid resolution 0.5–4 pc, are plotted in the first panel of Figure 1. Based on the diffusive timestep control, the dependence on resolution would be expected to be quadratic in the change in δx , such that the timestep for the $\delta x = 0.5$ pc run would be four times smaller than that of the $\delta x = 1$ pc run. In these relatively simple single SN expanding shocks, the magnitude of the viscous forces does not much exceed 10^6 and the timestep control is dominated by the artificial thermal diffusivity ζ_χ . From the second panel of Figure 1 it is evident that the maximal convergence, and therefore also ζ_χ , approximately halves for each doubling in resolution. This indicates that the explicit artificial diffusivities are inversely proportional to the grid resolution. Thus, the timestep appears to drop only linearly with grid cell size, rather than with the quadratic dependence expected for constant diffusivity.

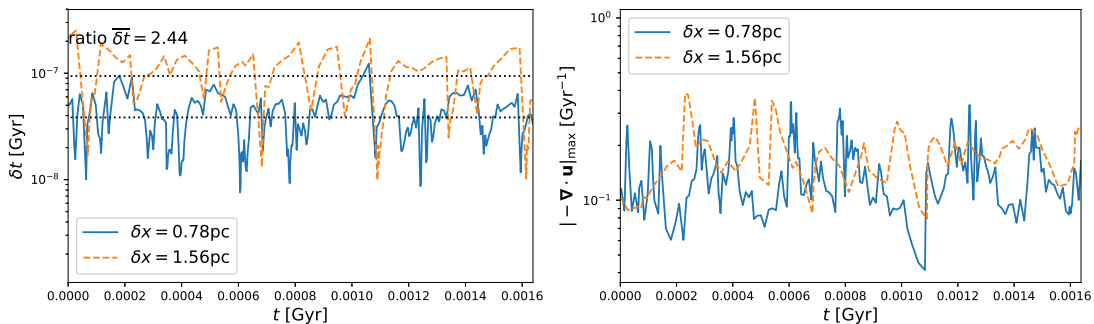


Figure 2. First panel: timestep evolution in SN driven turbulent simulations in unstratified periodic boxes with grid resolution of 1.56 and 0.78 pc. Dotted lines indicate the average timestep for each simulation. $D_{\text{shock}}, \nu_{\text{shock}}, \chi_{\text{shock}} = 1, 4, 4$. Second panel: evolution of the maximal value of convergence included in the artificial diffusion coefficients.

To demonstrate the effect on timestep in evolved turbulent systems, where the viscous forces and temperature gradients are large enough to impact the stability, the timestep and

maximum convergence are plotted in Figure 2 for simulations with grid spacing of 1.56 pc and 0.78 pc. The models apply random SN forcing to an unstratified magnetized ambient ISM with gas number density 1 cm^{-3} in a periodic slab. Stability requires that at each point the artificial diffusivities adopt the maximal value of the convergence with its two (rather than one) neighbours in either direction along each coordinate.

The time series are extracted from a statistical steady turbulent system, in which the magnetic field has saturated at a strength of a few μG . Temporal mean rms velocity, maximum velocity, and gas density and temperature extrema have similar values in each simulation. The timestep with the increased resolution is on average 2.44 times smaller. The magnitude of the maximal convergence displayed in the second panel of Figure 2 does not differ much due to resolution, as in the case of the single SN simulations. The drop in timestep remains approximately linear with grid cell size, but not due to lower strength of convergence. The control of the timestep is most often controlled by the gradients in the flow and the temperature. Both are typically higher with increased resolution, but the cost is again lower than the quadratic dependence associated with constant diffusivity.

3. Riemann shock tube test

3.1. Weak and moderate shocks

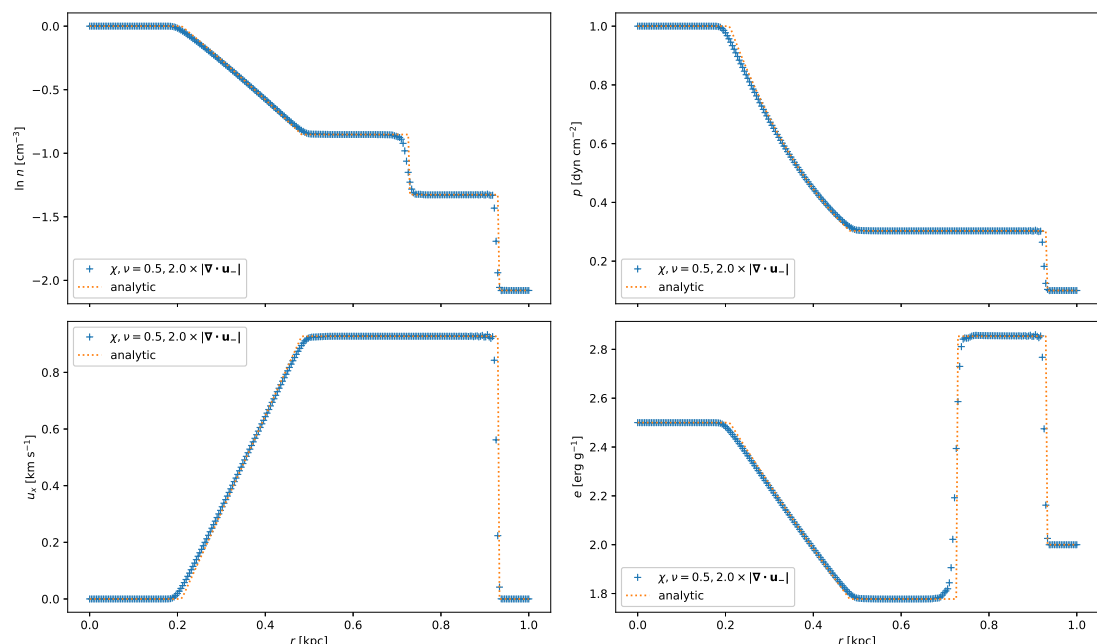


Figure 3. Results with 256 grid points for the weak Riemann shock tube test (Sod 1978) at $t = 0.245$, where the density, pressure on the left is initially set to $\rho, p = 1.0, 1.0$, and on the right $\rho, p = 0.125, 0.1$. Figures show gas number density, pressure, velocity and internal energy. The dotted line shows the analytic solution. The diffusivity coefficients used are $[D_{\text{shock}}, \nu_{\text{shock}}, \chi_{\text{shock}}] = [0, 2, 0.5]$.

To assess the quality of the shock handling scheme we consider the Riemann shock tube test using the standard setup described by Sod (1978), based on the exact analytical solution obtained by, e.g., Hawley *et al.* (1984). Results from a weak and a moderate shock test in a one dimensional grid over 256 points with closed boundaries are depicted in Figures 3 and 4, respectively. For direct comparison with Caunt and Korpi (2001, their Figures 11 and 12) we use the adiabatic index $\gamma = 1.4$. In each case an initial discontinuity in density and energy is

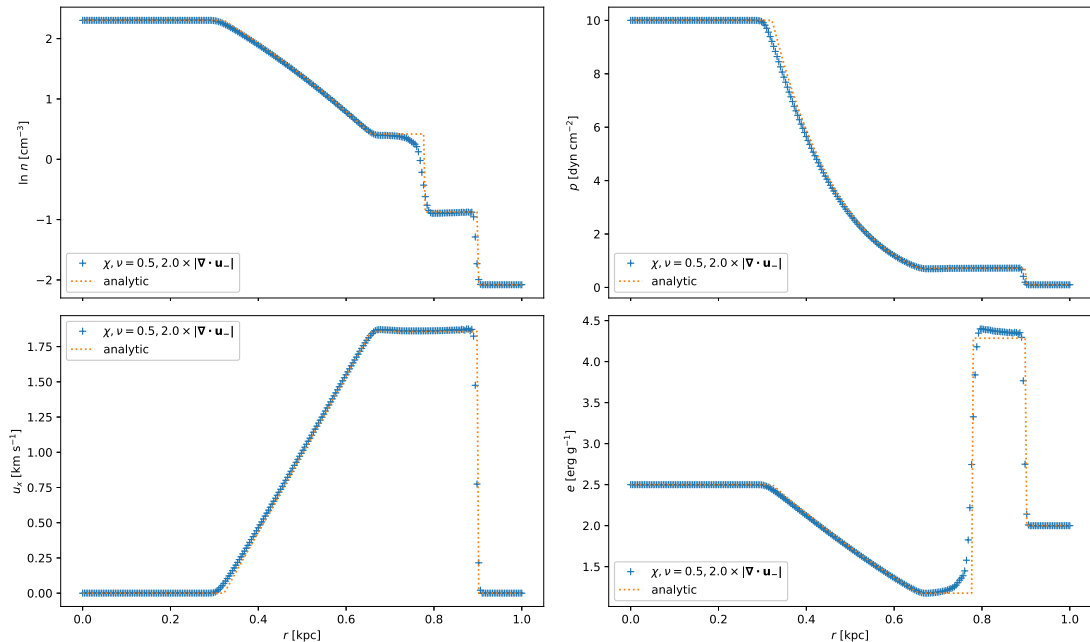


Figure 4. Results with 256 grid points for the moderate shock tube test (Sod 1978) at $t = 0.150$, where the density, pressure on the left is initially set to $\rho, p = 10.0, 10.0$, and on the right $\rho, p = 0.125, 0.1$. Figures show gas number density, pressure, velocity and internal energy. The dotted line shows the analytic solution. The diffusivity coefficients used are $[D_{\text{shock}}, \nu_{\text{shock}}, \chi_{\text{shock}}] = [0, 2, 0.5]$.

located at $r = 0.5$ with zero velocity, and on the right the dimensionless density and pressure are 0.125 and 0.1, respectively. In the weak shock in Figure 3 the density and pressure are both 1.0, and for the moderate shock in Figure 4 they are 10. The analytic solutions are displayed with dotted lines.

For these parameters, a reasonable solution can be obtained with the artificial diffusivities $\nu_{\text{shock}} = 2.0$ and $\chi_{\text{shock}} = 0.5$, and with no mass diffusion ($D_{\text{shock}} = 0$). However, if the initial discontinuity in mass and energy is not smoothed at all, then significant oscillations are evident in the wake of the shock, and for stronger shocks these can lead to artificial hot zones forming and crashing the code. In the weak and moderate shocks illustrated here, the initial profile is smoothed over an optimal five grid points, roughly the width over which the artificial viscosity resolves the developed shock. Less or more smoothing introduces numerical oscillations. In simulations of SN driven turbulence with SN shocks introduced to a highly nonuniform ambient ISM, we have no such fine tuning over the level of discontinuity smoothing, so for the stronger shock test below we apply minimal smoothing across three grid points and enhance the artificial diffusivity further to be less sensitive to such effects.

In Figure 3, we see the main deviation from the analytic solution is smoothing at the transitions on either side of discontinuities, most evident in the plots for gas density and internal energy. With increasing resolution, which we explore in Section 3.2, the numerical solution asymptotically approaches the analytic solution. The Mach number in this experiment peaks just above 1.

As we move to a moderate shock, peaking above Mach 2.5, we see in Figure 4 that the artificial viscosity scheme is vulnerable to additional numerical artifacts, particularly in the density and energy profiles. At the rear of the leading shock block, the energy has a peak and the density a dip. This is the region in the numerical scheme, where there is the most vulnerability to numerical instability. Note that at these locations the divergence of the flow is zero, so no diffusivity is applied. Hence the smoothing of density in the post-shock gas near $r = 0.8$ is an historical inheritance of the viscosity applying earlier in its evolution. The

velocity and pressure are constant between about $r = 0.65$ and $r = 0.9$, while the density due to the smoothing is reduced compared to the analytic solution, and hence the gas is hotter.

3.2. High Mach number shock

The standard shock tube tests indicate that the code can adequately cope with weakly compressible flows. For shocks associated with SN driven turbulence, however, this is not sufficient. Simulations of the ISM commonly include minimal temperatures near 100 K (sound speed 0.5 km s^{-1}) and maximal velocities above 1000 km s^{-1} . Even if we exclude the improbable extrema Mach 2000 associated with SN explosions deep within molecular clouds, we regularly encounter Mach 100 shocks in these simulations, depending on the ambient temperature around each SN location.

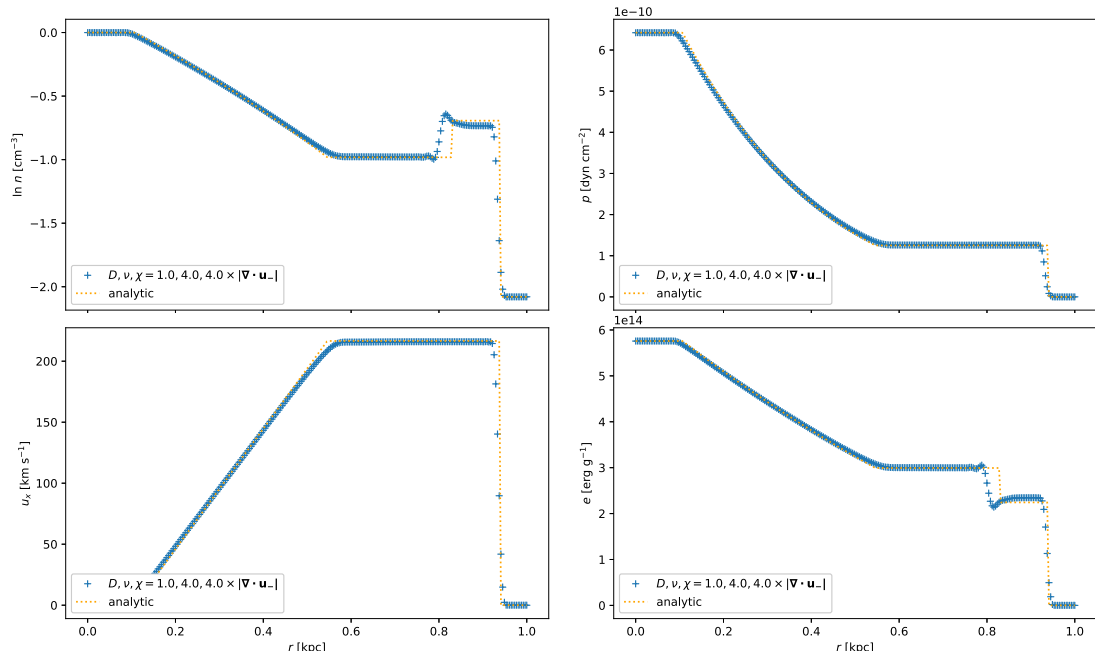


Figure 5. Results with 256 grid points for the high Mach number Riemann shock tube test (Sod 1978) at $t = 0.005$, where the density, pressure on the left is initially set to ρ , $p = 1.0$, $6.4 \cdot 10^{-10}$, and on the right ρ , $p = 0.125$, $4.8 \cdot 10^{-15}$. Figures show gas number density, pressure, velocity and internal energy. The dotted line shows the analytic solution. The diffusivity coefficients used are $[D_{\text{shock}}, \nu_{\text{shock}}, \chi_{\text{shock}}] = [1, 4, 4]$.

In Figure 5 we show the results of a Riemann shock test exceeding Mach 100. The adiabatic index is $5/3$. The pressure discontinuity is about five orders of magnitude. As well as increasing the artificial viscosity and thermal diffusivity coefficients to $\nu_{\text{shock}} = 4.0$, $\chi_{\text{shock}} = 4.0$, we also include an artificial diffusion to the continuity equation, as described in Section 2.3. In this example we set $D_{\text{shock}} = 1.0$.

In the density profile of Figure 5 there is a small overshoot in energy behind the shock, accompanied by some numerical oscillation at the contact discontinuity. Whether the spikes or dips are the larger depends on the level of smoothing relative to the strength of the discontinuity profile. As mentioned earlier, we have little control on the structure of the shock injections in the turbulent ISM environment, so we expect some such artifacts to be present, but choose coefficients to optimally dampen such oscillations. The post-shock density does not quite reach the analytic value.

We consider the effect of resolution in Figure 6, by zooming in on the shock front at this same moment in its evolution. We see that the reduction in post-shock density from the

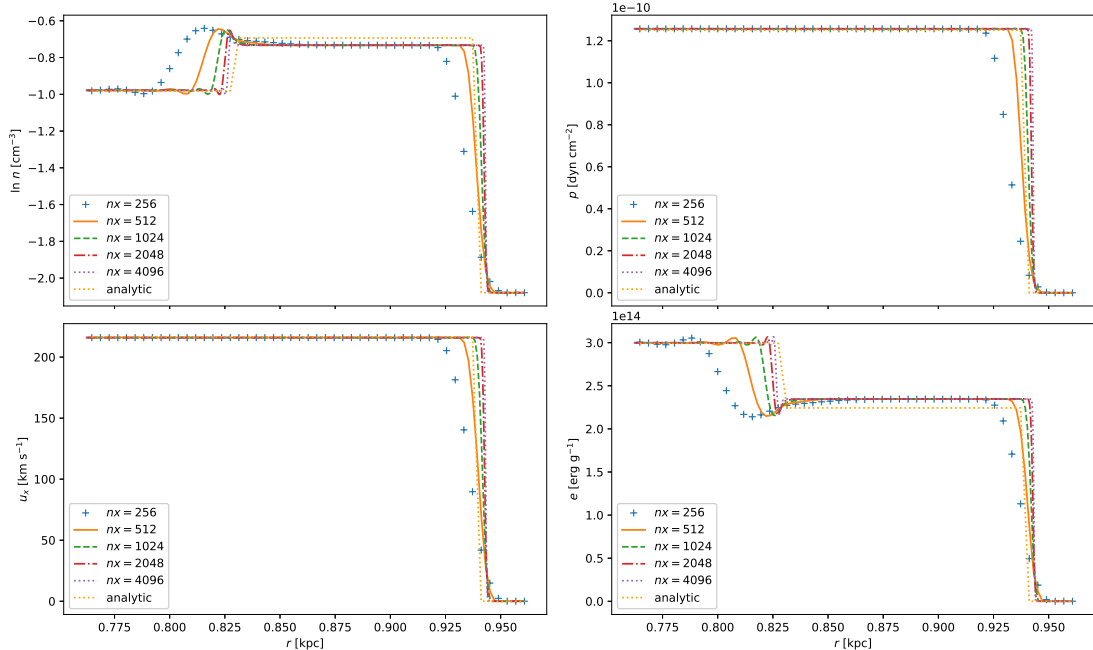


Figure 6. Results for various grid resolutions (256–4096 grid points) for the high Mach number Riemann shock tube test shown in Figure 5. Figures show gas number density, pressure, velocity and internal energy. The dotted line shows the analytic solution. The diffusivity coefficients used are $[D_{\text{shock}}, \nu_{\text{shock}}, \chi_{\text{shock}}] = [1, 4, 4]$.

analytic solution does not change with resolution. As the resolution increases, the distribution converges to a profile more closely aligned with the analytical solution, more evenly dispersed on either side of the shock front. We shall show in Section 3.3 that this asymptotic disparity with the analytic result is due to the mass diffusion term.

3.3. Dependence on diffusivity and mass diffusion correction

The analytic solutions to the weak and moderate shock tube tests are reasonably satisfied with modest artificial viscosity and artificial thermal diffusivity, without any requirement to introduce artificial mass diffusion to the continuity equation. First we shall consider the effects of the two former applications of diffusivity on the numerical solution and then we shall discuss the motivation and consequences of adopting mass diffusion.

When we consider the effect of the artificial viscosity for the strong shock tube test (Mach 100), illustrated in Figure 7, we see that for $\nu_{\text{shock}} = 1.0$ there are artificial extrema and oscillations in all variables. This is most evident in the velocity profile. For lower ν_{shock} values the velocity and pressure shock fronts are ahead of the analytic solution and the post-shock density also drops. As the viscosity coefficient increases the solution approaches the analytic value for the post-shock density. The shock broadens in all variables as the coefficient increases, but as seen in the resolution comparisons of Figure 6, the solution improves as resolution increases.

The effect of increasing ν_{shock} from 4 to 8 is minor, however. Even for very high values the change is weak, except that the leading shock edge in all variables broadens due to the undesirable additional diffusion. There is a benefit in adopting a value between about 4 and 10. These solutions adequately suppress the wiggles in the wake of the shock. Larger values would have a negative impact on the diffusive time step and can increase the viscous forces or viscous heating locally. High forces and heating resulting from this can be detrimental to the code stability as discussed in Section 2.4.

Now consider the dependence of the solution on the shock thermal conductivity χ_{shock}

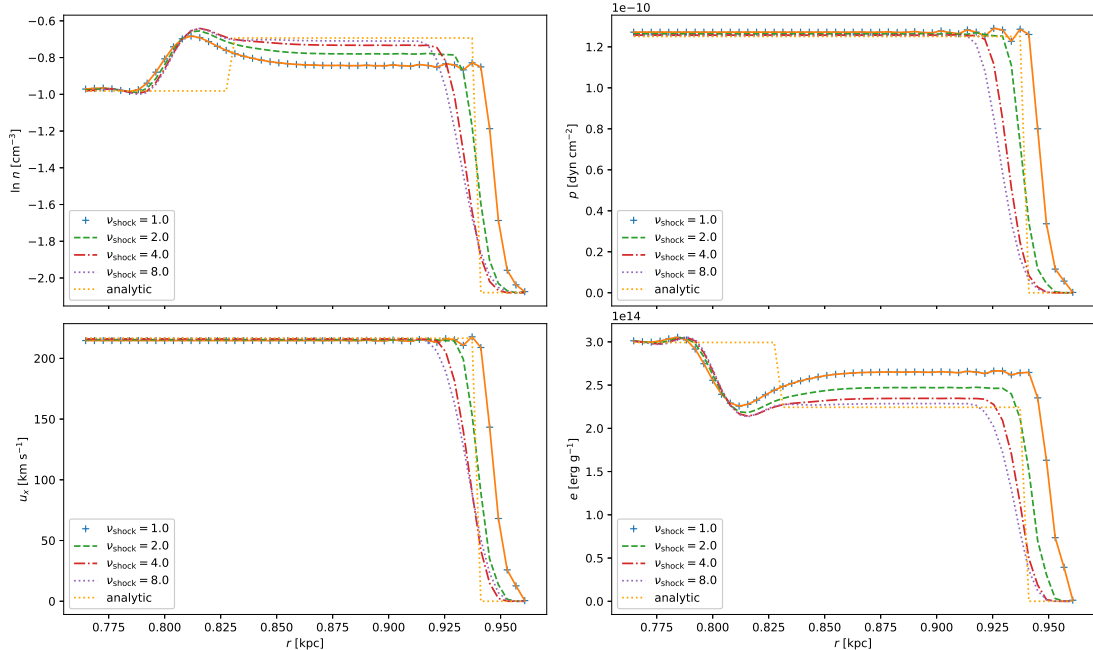


Figure 7. Results with 256 grid points for the high Mach number Riemann shock tube test (Sod 1978) at $t = 0.005$, where the density, pressure on the left is initially set to $\rho, p = 1.0, 6.4 \cdot 10^{-10}$, and on the right $\rho, p = 0.125, 4.8 \cdot 10^{-15}$. Figures show gas number density, pressure, velocity and internal energy. Solutions for shock viscosity coefficient $\nu_{\text{shock}} = 0, 1, 2, 4, 8$ are compared to the analytic solution zoomed in near the shock front. The other diffusivity coefficients are fixed at $[D_{\text{shock}}, \chi_{\text{shock}}] = [1, 4]$.

shown in Figure 8. In all profiles we find weak dependence on the strength of χ_{shock} . As χ_{shock} increases the density extrema in the wake of the shock are smoothed, but the post-shock density remains unchanged. For pressure and energy the numerical shock front is more diffused ahead of the analytic shock as χ_{shock} increases.

The solution varies more weakly as χ_{shock} increases. The nose of the shock front moves further ahead of the analytic solution for high χ_{shock} . At the contact discontinuity, the amplitude of the artificial extrema reduces slightly as χ_{shock} increases. For saturation values of χ_{shock} the contact discontinuity shifts back to about $r = 0.79$.

Compared to the dependence on artificial viscosity, increases beyond $\chi_{\text{shock}} = 4$ or 8 appear to cause less additional diffusion. These values do not appear strongly advantageous over values of 1 and 2, yet we know from experiments with SN turbulence and the higher resolution snowplough tests reported in Section 4 that the slightly larger oscillations illustrated in the density profile for $\chi_{\text{shock}} = 0$, are sufficient to lead to numerical instability. We recommend a nonzero value of χ_{shock} , for moderately compressible turbulence $\chi_{\text{shock}} \gtrsim 1.0$ and for highly compressible turbulence $\chi_{\text{shock}} \gtrsim 4.0$. Higher values should be avoided to limit diffusion, particularly in energy.

In Figure 9 we display results for varying values of D_{shock} . When this is set to zero, the lag in the position of the shock front is largest, but the post-shock density approaches the analytic value most closely. There does not appear to be convergence to an asymptotic profile as D_{shock} increases, with tests using values above 50 showing greater diffusion at both the shock and the contact discontinuity. Larger magnitude extrema at the contact discontinuity may even appear for higher values. Therefore, $D_{\text{shock}} \simeq 1$ or 2 is recommended and appears sufficient to avoid numerical instability.

We conclude from this analysis that modest artificial viscosity and thermal diffusivity allow a reasonable representation of adiabatic shocks with high Mach number. The lag in shock position and thickness of the shock front in the lowest resolution runs are not significantly

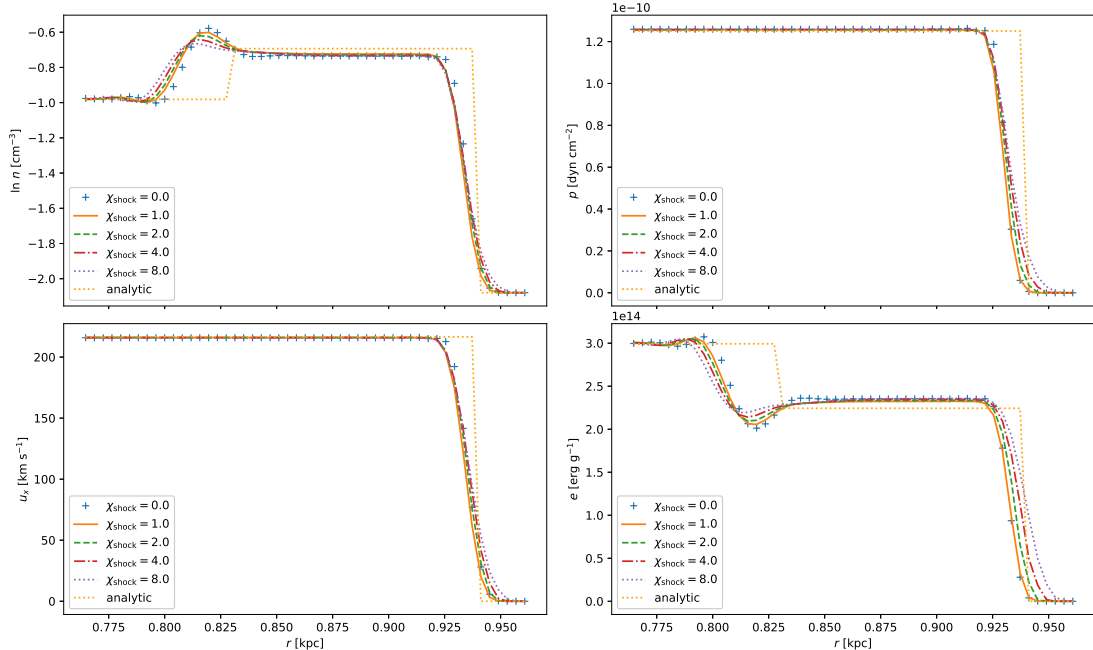


Figure 8. Results with 256 grid points for the high Mach number Riemann shock tube shown in Figure 5. Figures show gas number density, pressure, velocity and internal energy. Solutions for shock thermal diffusivity coefficient $\chi_{\text{shock}} = 0, 1, 2, 4, 8$ are compared to the analytic solution zoomed in near the shock front. The other diffusivity coefficients are fixed at $[D_{\text{shock}}, \nu_{\text{shock}}] = [1, 4]$.

dependent on the values of the diffusion coefficients, and are both resolution artifacts. The mass diffusion spreads the mass in the shock front beyond the analytic region. Numerical instability in the full turbulent simulations seems to occur at interacting shocks that produce wall heating and density deficits. Inclusion of mass diffusion likely regularizes these points, inhibiting numerical instability.

4. 3D supernova remnants

Previous tests of SN modelling with the Pencil Code are reported in Gent (2012, Appendix A). These included higher diffusivities and suppression of the cooling in shock fronts. We now use access to greater computational resources to apply the tests across a wider range of ambient densities and grid resolution, with timestep control, the improved treatment of artificial viscosity described here, and without unphysical suppression of radiative cooling. Numerical results are compared with analytic solutions for an SN remnant expanding into a perfect, homogeneous, monatomic gas at rest.

The SN energy is injected into the existing density distribution in a sphere with an initial nominal radius of 17 pc (4.25 grid spaces). The energy injection radial profile follows

$$E(R) = E_0 \exp \left(- \left[\frac{R}{0.0017 \text{ kpc}} \right]^4 \right), \quad (13)$$

with normalising coefficient E_0 set such that the volume integral of $E(R)$ is 10^{51} erg. This provides a sufficiently smooth initial shock front, which can also be handled in a highly nonuniform turbulent injection site, while the remnant formed has a reasonably uniform internal temperature.

Although the minimum initial radius is 4.25 grid spaces, a further constraint is to expand the injection radius to ensure at least $25M_{\odot}$ is present. Consequently the 0.001 cm^{-3} model

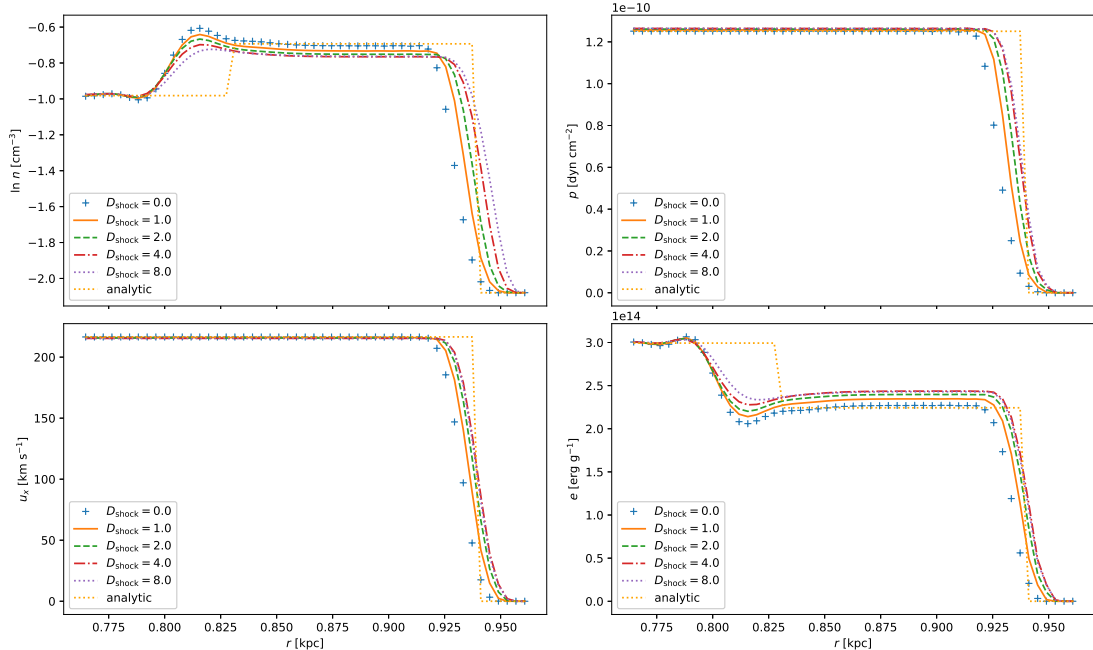


Figure 9. Results with 256 grid points for the high Mach number Riemann shock tube shown in Figure 5. Figures show gas number density, pressure, velocity and internal energy. Solutions for mass shock diffusion coefficient $D_{\text{shock}} = 0, 1, 2, 4, 8$ are compared to the analytic solution zoomed in near the shock front. The other diffusivity coefficients are fixed at $[\nu_{\text{shock}}, \chi_{\text{shock}}] = [4, 4]$.

has an initial radius of 62 pc. For these tests, the low density models can cope with smaller injection radii, but in the turbulent system we need to ensure there is enough total mass to avoid local numerical instability. Some authors avoid the additional complications of turbulent injections sites by smoothing the gas to a uniform density. For example, Joung and Mac Low (2006) adjust the radius to enclose $60M_{\odot}$, then smooth the volume to a uniform density. To handle explosions in high density regions, where cooling can inhibit the power of the SN one solution is simply to delete enough mass inside the injection site to allow high enough temperature or to move the mass to the remnant shell at injection. So far, we have been able to avoid such measures and, particularly when evolving the dynamo, would prefer not to unphysically remove the gas from the magnetic field or consider also rearranging the ambient potential field.

4.1. Adiabatic remnant

The early stages of SN evolution are approximately adiabatic. For a uniform ambient medium they are well described by the Sedov-Taylor analytic solution (Taylor 1950, Sedov 1959),

$$R = \left(\kappa \frac{E_{\text{SN}}}{\rho_0} \right)^{1/5} t^{2/5}, \quad (14)$$

where R is the remnant radius, E_{SN} the explosion energy, ρ_0 the ambient gas density, and the dimensionless parameter $\kappa \approx 2.026$ for $\gamma = 5/3$ (Ostriker and McKee 1988).

In Figure 10 for a range of ambient ISM densities we compare the radial evolution of the remnant shell between our numerical models and the analytic solution described by Equation (14). The coefficients used are $D_{\text{shock}}, \nu_{\text{shock}}, \chi_{\text{shock}} = 5, 5, 5$. The power law growth of the radius is in reasonable agreement with the analytic prediction, although the numerical solutions are slightly fast. This is consistent with the analysis above of the strong shock tube tests. We also include results for ambient density of 1 cm^{-3} with the shock coefficients set to

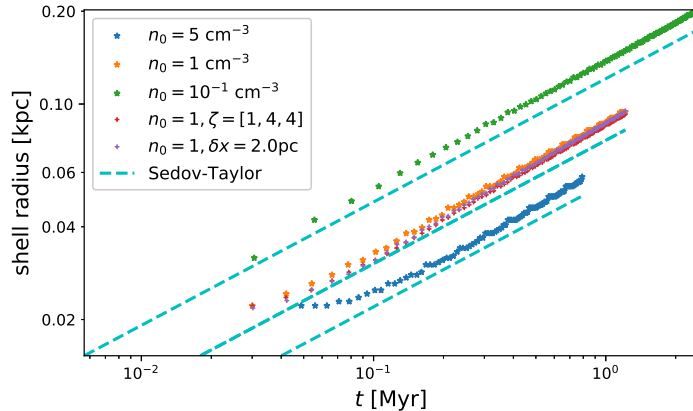


Figure 10. Time evolution of remnant shell radius in the adiabatic Sedov-Taylor regime for ambient gas number density between 0.1 and 5 cm^{-3} with resolution along each side of 4 pc . The diffusivity coefficients used are $[D_{\text{shock}}, \nu_{\text{shock}}, \chi_{\text{shock}}] = [5, 5, 5]$. For comparison examples at 1 cm^{-3} are also included with $[D_{\text{shock}}, \nu_{\text{shock}}, \chi_{\text{shock}}] = [1, 4, 4]$ and resolution 2 pc marked with red crosses.

[1,4,4] (red crosses) and grid resolution of 2 pc (purple crosses), and observe that the higher precision numerical solutions approach the analytic ones, at least in the early phase of the remnant evolution.

4.2. Momentum conserving, pressure driven and momentum driven snowplough

When radiative cooling processes are included the SN evolution changes. As the remnant expands and the shock front accumulates more gas from the ambient ISM, cooling becomes more efficient in the increasingly dense shell. With the loss of energy the shell speed falls. The standard momentum-conserving snowplough solution for a radiative SN remnant has the form

$$R = R_0 \left[1 + 4 \frac{\dot{R}_0}{R_0} (t - t_0) \right]^{1/4}, \quad (15)$$

where R_0 is the radius of the SN remnant at the time t_0 of the transition from the adiabatic stage, and \dot{R}_0 is the shell expansion speed at t_0 . The transition time is determined by Woltjer (1972) to align with half of the SN energy being lost to radiation; this happens when

$$\dot{R}_0 = 230 \text{ km s}^{-1} \left(\frac{n_0}{1 \text{ cm}^{-3}} \right)^{2/17} \left(\frac{E_{\text{SN}}}{10^{51} \text{ erg}} \right)^{1/17}, \quad (16)$$

with n_0 the gas number density of the ambient ISM. The transitional expansion speed thus depends very weakly on parameters.

Cioffi *et al.* (1988) obtained numerical and analytical solutions for an expanding SN remnant with special attention to the transition from the Sedov–Taylor stage to the radiative stage. These authors adjusted an analytical solution for the pressure-driven snowplough stage to fit their numerical results to an accuracy of within 2% and 5% in terms of R and \dot{R} , respectively. (Their numerical resolution was 0.1 pc in the interstellar gas and 0.01 pc within ejecta.) They thus obtained

$$R = R_p \left(\frac{4}{3} \frac{t}{t_p} - \frac{1}{3} \right)^{3/10}, \quad (17)$$

where the subscript p denotes the radius and time for the transition to the pressure driven stage. The estimated time of this transition is

$$t_p \simeq 13 \text{ Myr} \left(\frac{E_{\text{SN}}}{10^{51} \text{ erg}} \right)^{3/14} \left(\frac{n_0}{1 \text{ cm}^{-3}} \right)^{-4/7}. \quad (18)$$

This continues into the momentum driven stage with

$$\left(\frac{R}{R_p} \right)^4 = \frac{3.63}{t_p} \left(t - t_m \right) \left[1.29 - \left(\frac{t_p}{t_m} \right)^{0.17} \right] + \left(\frac{R_m}{R_p} \right)^4, \quad (19)$$

where subscript m denotes the radius and time for this second transition,

$$R_m^4 = 4.66 \frac{t}{t_p} \left[1 - 0.939 \left(\frac{t}{t_p} \right)^{-0.17} + 0.153 \left(\frac{t}{t_p} \right)^{-1} \right] \quad (20)$$

and

$$t_m \simeq 61 t_p \left(\frac{\dot{R}_{\text{ej}}}{10^3 \text{ km s}^{-1}} \right)^3 \left(\frac{E_{\text{SN}}}{10^{51} \text{ erg}} \right)^{-3/14} \left(\frac{n_0}{1 \text{ cm}^{-3}} \right)^{-3/7}, \quad (21)$$

where $\dot{R}_{\text{ej}} \simeq 5000 \text{ km s}^{-1}$ is the initial velocity of the $4M_{\odot}$ ejecta. The shell momentum in the latter solution tends to a constant, and the solution thus converges with the momentum-conserving snowplough Equation (15); but, depending on the ambient density, the expansion may become subsonic and the remnant merge with the ISM beforehand.

These profiles are computed for the ambient densities $n_0 = (0.001, 0.01, 0.1, 1, 5) \text{ cm}^{-3}$ used in the tests reported here. Although these semi-analytical models are a useful comparison to examine the accuracy of our numerical models, there are differences to consider. The Cioffi *et al.* (1988) 1D analysis was conducted for ambient IS with number density 0.1 cm^{-3} and ambient temperature 10 K to ensure the blast wave remained strong; their cooling follows a different piecewise power-law fit (Raymond *et al.* 1976), and is truncated at $1.2 \cdot 10^4 \text{ K}$; and they do not include UV heating. They use resolution 0.1 pc outside the remnant, and 0.01 pc to resolve the ejecta. Because heating and cooling apply in our models at lower temperatures, for each density and each cooling function the ambient temperature is set at thermal equilibrium, so the external pressure remains constant over time.

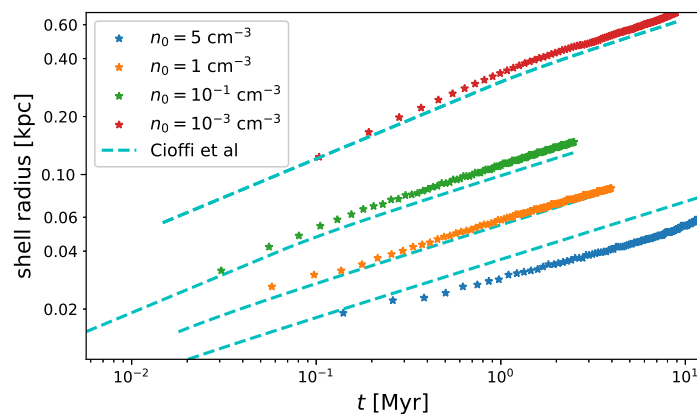


Figure 11. Time evolution of remnant shell radius following cooling function of Rosen *et al.* (1993) for ambient gas number density between 0.001 and 5 cm^{-3} with grid cell resolution of 4 pc . The diffusivity coefficients used are $[D_{\text{shock}}, \nu_{\text{shock}}, \chi_{\text{shock}}] = [5, 5, 5]$.

The Pencil Code currently has two implementations of radiative cooling associated with SN turbulence, both based on piecewise power law dependence on temperature. These are

described in Gent *et al.* (2013a, see their Figure 1) and are based on Rosen *et al.* (1993) and a combination of Wolfire *et al.* (1995) and Sarazin and White (1987). Results for the former are illustrated in Figure 11. The power law is a good fit for the ambient density 0.1 cm^{-3} , most closely matching the Cioffi *et al.* (1988) setup, although the shell radius is somewhat overestimated in our model.

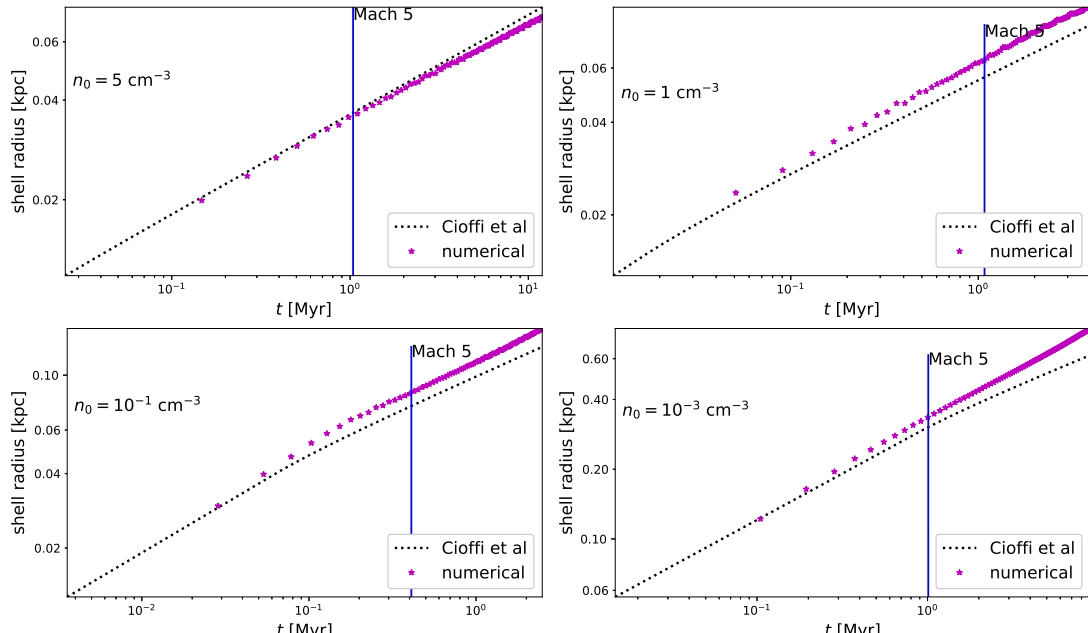


Figure 12. Time evolution of remnant shell radius following cooling function of Wolfire *et al.* (1995) and Sarazin and White (1987) for ambient gas number density between 10^{-3} and 5 cm^{-3} at grid resolution of 4 pc. Snowplough and Cioffi *et al.* (1988) analytic solutions are indicated for comparison. The diffusivity coefficients used are $[D_{\text{shock}}, \nu_{\text{shock}}, \chi_{\text{shock}}] = [1, 4, 4]$.

The cooling at high temperatures is higher for the Rosen *et al.* (1993) model than the Sarazin and White (1987) model, so it is understandable that the remnants in the latter case would evolve faster. In Figure 12 we see that the remnant shells are expanding faster than in the Rosen *et al.* (1993) models. This is with reduced $D_{\text{shock}}, \nu_{\text{shock}}, \chi_{\text{shock}} = 1, 4, 4$. For the diffusivities of 5,5,5 (not shown) the overshoot was higher, except in the first panel for ambient density 5 cm^{-3} , which followed an evolution slower than the snowplough analytic solution. With this cooling function the initial radius of injection was 14 pc. In earlier experiments 17 pc was used, to avoid angular features appearing from the Cartesian grid. The change had negligible effect on the features of the remnants, other than for the 5 cm^{-3} model, which benefitted from reduced cooling in the early stages. The time at which the remnant reaches Mach 5 is added to indicate how close the numerical solution is to the analytic solution when the remnant is near to becoming subsonic with respect to the ambient medium.

The relationship between cooling, temperature and density is nonlinear, so it is not clear that the relations derived by Cioffi *et al.* (1988) for 0.1 cm^{-3} ambient ISM should also apply for the other densities. Nonetheless the results for lower densities seem reasonable. For higher densities (above 1 cm^{-3}) at this resolution, a smaller radius is required. Cooling is most efficient around 10^5 K , so the initial temperature needs to exceed 10^6 K to prevent energy losses too early in the remnant evolution. Increasing resolution and reducing the diffusivity coefficients improves the agreement between numerical and analytic solutions. Indeed, this assertion was borne out by models with the latter cooling function being run with both sets of coefficients, and the 5 cm^{-3} model with an initial radius of 14 pc (3.5 grid spaces).

4.3. Effects of ambient density, resolution and diffusivity

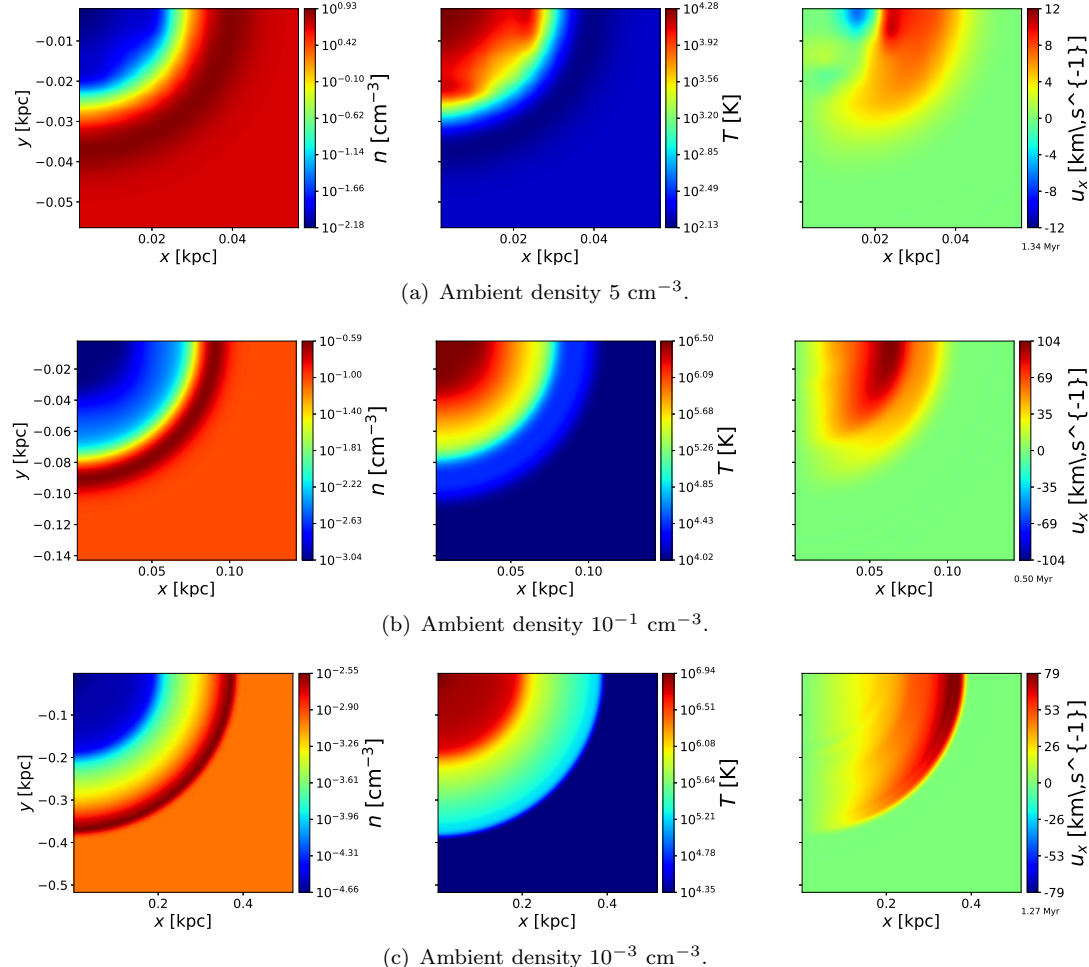


Figure 13. 2D quarter-slices from the $z = 0$ plane depicting gas number density, temperature and x -component of velocity. Ambient gas number density in each figure is 5, 0.1 and 0.01 cm^{-3} and each snapshot corresponds to the time at which the remnant shell speed falls to Mach 5 for the ambient ISM. The diffusivity coefficients used are $[D_{\text{shock}}, \nu_{\text{shock}}, \chi_{\text{shock}}] = [1, 4, 4]$.

Snapshots of the remnant density, temperature and velocity distributions at 4 pc resolution for ambient densities 5, 0.1 and 0.01 cm^{-3} are displayed in Figure 13. The 3D simulations are on a Cartesian grid, with the SN origin at $\mathbf{0}$. As the profile is symmetric, unnecessary duplication is avoided by displaying a quarter plane. The snapshots are at times when the shell expansion is near Mach 5. In the second panel, top row, the cooling shell is visible for 5 cm^{-3} as it drops to lower temperature than the ambient medium, whereas in the lower density runs the shell cooling has not yet begun.

For ambient density 1 cm^{-3} we explore the effects of resolution. At this density the thermal equilibrium with the Wolfire *et al.* (1995) and Sarazin and White (1987) combination of cooling and heating occurs at about 2185 K, which is on a thermally unstable branch of the cooling curve. In developing the numerical model this density proved to be more vulnerable to instabilities than either lower or higher densities. It therefore was of most interest for the resolution tests.

In Figure 14 we compare the time evolution of the shell radius for grid resolutions of 0.5–4 pc at ambient density 1 cm^{-3} . A linear y -scale is used to better display the differences. There is convergence towards the analytic result with increasing resolution.

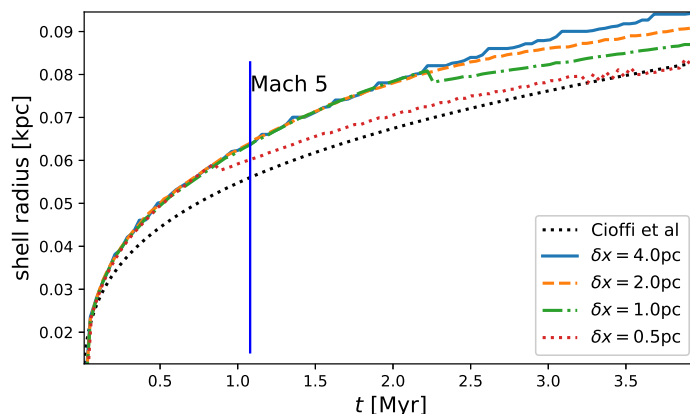


Figure 14. Time evolution of remnant shell radius following cooling function of Wolfire *et al.* (1995) and Sarazin and White (1987) for unit ambient density at grid resolution of 0.5–4 pc. With increasing resolution the numerical solution converges to the semi-analytic solution of Cioffi *et al.* (1988, black, dotted). The diffusivity coefficients used are $[D_{\text{shock}}, \nu_{\text{shock}}, \chi_{\text{shock}}] = [1, 4, 4]$.

There are two remaining issues that may affect this diagnostic. First, although the higher resolution model remnant injecta could be resolved with fewer grid points, all models use the same injection radius of 14 pc, to isolate the effects of resolution. This may explain why the higher resolution models appear to converge to the analytic solution best at later times: the initial radius is not the most appropriate for these models. Second, locating the remnant shell radius from any given snapshot is not precise. The method used here is to collect all locations that match the peak density, and then compute their mean radius from the origin. Due to the discrete nature of the grid and the shocked shell spanning 3–5 grid spacings, the maxima also move unevenly. In the 0.5 pc (red,dotted) and 1 pc (green, dash-dotted) resolution runs the shell front is computed to reverse at about 1 Myr and 2.3 Myr, respectively. Close inspection of the shock wave evolution across these snapshots, reveals a wave resolved over 5 or so grid points, in which the peak is initially immediately behind the shock front. While the whole shell continues to move forward, cooling within the shell causes the density at the contact discontinuity to grow larger than the post-shock density so that this then replaces the leading edge as the peak, moving the estimated radius back 1–1.5 pc or 2–3 pc, respectively.

Slices of snapshots from these runs while the shell is expanding at Mach 5 into the ambient ISM are displayed in Figure 15. At 4 pc resolution middle panel (a) we see that the shell has not yet started to cool below the ambient ISM temperature, while at 1 pc and even 2 pc, cooling is occurring. In previous Pencil Code SN driven turbulence at 4 pc resolution cold gas below 100 K was present, but this result suggests they arose primarily from compression fronts at remnant interactions and general turbulent shocks.

The thickness of the shell density is common across resolution, but more sharply defined as the resolution increases, which is consistent with the resolution analysis of the strong shock tube in Section 3.2. The reverse shocks (blue) in the velocity panels (a) and (b) occur because the ambient pressure is non-zero, and the energy input is not an idealized point source. In the diffuse interior with low momentum these velocities can be higher than the remnant shell speed. The effect reduces with resolution, since the coarse Cartesian grid defining the injection sphere exacerbates this effect.

Slices of the highest resolution model of 0.5 pc grid spacing are shown in Figure 16 for snapshots at the time when the shell reaches Mach 5 and at twice that elapsed time. In addition to the features present at 1 pc resolution, we see the emergence of the Vishniac-Ostriker-Bertschinger (Vishniac 1983, Vishniac *et al.* 1985) overstability arising from the cooling reducing the thickness of the shell. At Mach 5 the overstability can be seen entering the nonlinear phase in the thin, dense, cooled shell (see Mac Low and Norman 1993, for

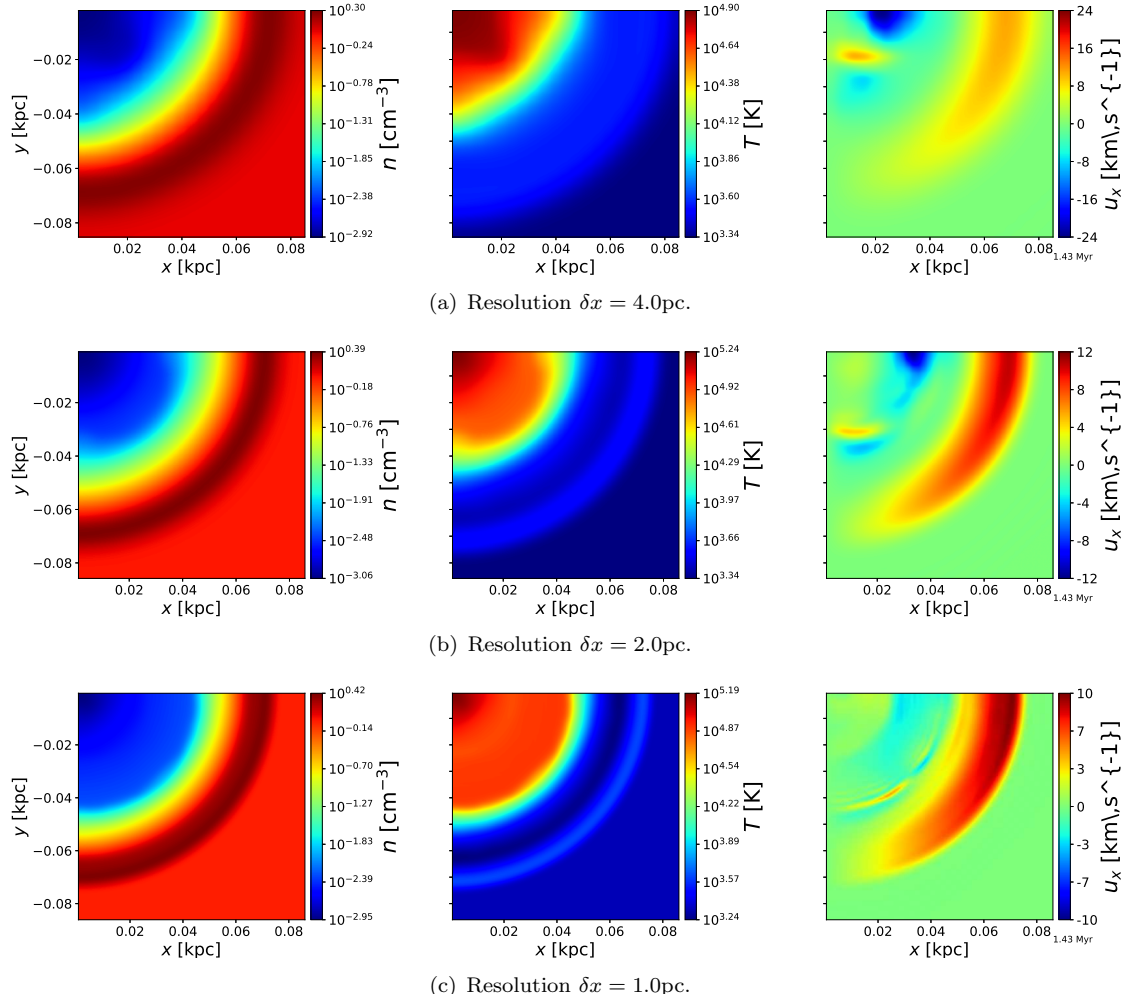


Figure 15. 2D quarter-slices from the $z = 0$ plane depicting gas number density, temperature and x -component of velocity. Ambient gas number density in each figure is 1 cm^{-3} and the resolution along each edge 4, 2 and 1 parsecs, respectively. The diffusivity coefficients used are $[D_{\text{shock}}, \nu_{\text{shock}}, \chi_{\text{shock}}] = [1, 4, 4]$.

a detailed analysis). The later snapshot is included to show this effect as it evolves further in all variables. Tests show that using $D_{\text{shock}}, \nu_{\text{shock}}, \chi_{\text{shock}} = 5, 5, 5$ suppresses the overstability, but $D_{\text{shock}}, \nu_{\text{shock}}, \chi_{\text{shock}} = 1, 4, 4$ allows it to appear as shown in Figure 16.

5. Summary of results

In order to stabilize shocks in the high-order Pencil code, we have demonstrated the use of a von Neumann artificial viscosity, as implemented for example by Stone and Norman (1992), in combination with the application at the shock front of artificial thermal diffusivity and mass diffusion to the energy and continuity equations. This combination reduces the vulnerability of the Pencil Code to numerical instability while significantly reducing the overall diffusivity of the model previously applied by Gent (2012) to SN driven turbulence in the ISM. The inclusion of artificial mass diffusion alters the determination of momentum and energy, and we implement a correction term to each equation to consistently conserve their properties. Similar artificial mass diffusion has been applied by, Ryutov *et al.* (for example, 2005), Johansen *et al.* (for example, 2006, 2009), but without explicit corrections to the momentum and energy equations.

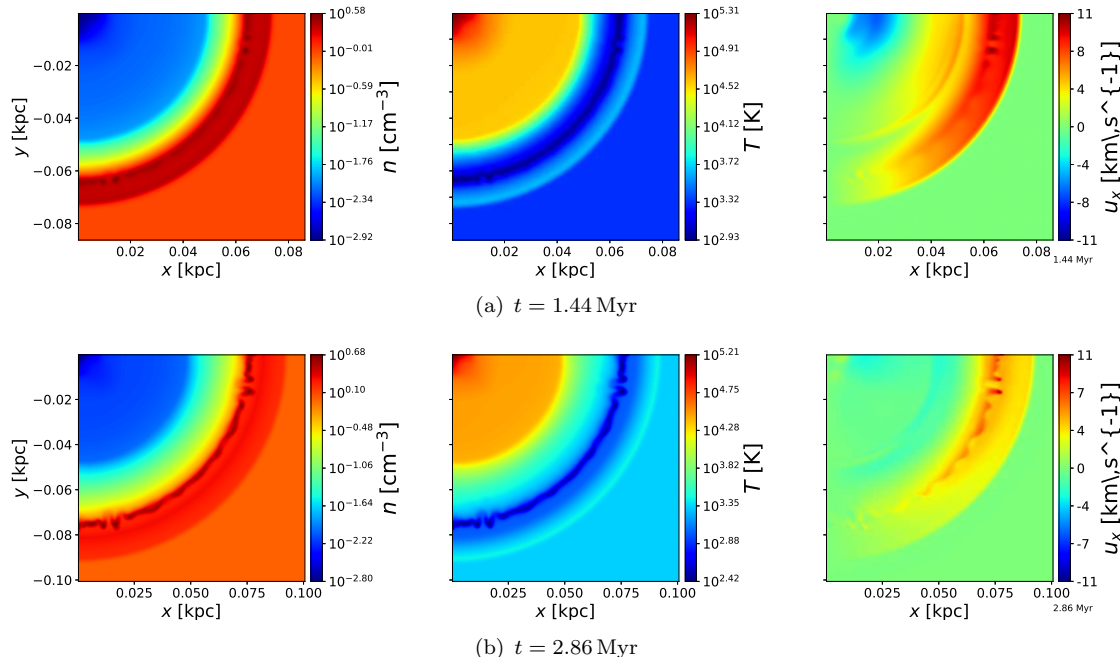


Figure 16. 2D quarter-slices from the $z = 0$ plane depicting gas number density, temperature and x -component of velocity. The top panel shows the shell as its Mach number reaches 5, while the bottom panel shows developed Vishniac-Ostriker-Bertschinger instability. Ambient gas number density is 1 cm^{-3} and the grid resolution is 0.5 pc. The diffusivity coefficients used are $[D_{\text{shock}}, \nu_{\text{shock}}, \chi_{\text{shock}}] = [1, 4, 4]$.

We have also introduced additional tools for controlling the timestep depending on the sum of all terms on the right hand side of the momentum equation and the energy equation. These stabilize the code by constraining the time step based on the maximal change in time at each iteration. Empirically, we find the viscous forces, viscous heating and temperature gradients tend to be extremely high in the SN turbulence, and can introduce numerical instabilities if the timestep is not sufficiently small to resolve the time evolution. The alternative of just reducing the Courant number for the diffusive timestep may work, but as it is based on the diffusion coefficients alone would tend to reduce the timestep more universally, therefore slowing the code at every iteration. The adaption to the maximal forces or heating acts only when they are largest, often in the aftermath of an SN, so the timestep can recover subsequently. Another advantage is that the timestep can be less sensitive to decreases in grid spacing compared to the diffusive timestep, which scales inversely with the square of the grid spacing. This is because the unified time steps tend to be proportional to the size of the cell-to-cell velocity gradients, which decrease with decreasing cell size. Hence, increases in resolution need not be so comparatively numerically expensive.

The code reaches reasonable agreement with the Riemann shock tube test for shocks exceeding Mach 100 for a range of resolutions. A minimum value of $\nu_{\text{shock}} = 3$ is required for the artificial viscosity coefficient for such high Mach numbers and some artificial thermal diffusivity is required to dampen instabilities in the wake of the shock front. The replication of the strong shock profile is relatively insensitive to changes in the coefficients ν_{shock} and χ_{shock} , in the range 2–8. Grid resolution, rather than the size of the artificial diffusivity coefficients, is the primary determinant of the level of smoothing present in the numerical shock profiles. The divergence of the flow is inversely proportional to the grid size, so the effective artificial diffusivity as function of resolution scales approximately as $\nu_{\text{shock}} \delta x^{-1}$.

The capacity of the code to model SN blast waves was tested against the Sedov-Taylor analytic and Cioffi *et al.* (1988) semi-analytic solutions. Simulations were evolved until the blast wave becomes subsonic with respect to the ambient ISM. The models give good agreement

with the Sedov-Taylor $t^{2/5}$ power law for the SN remnant shell radius evolution over a range of ambient ISM gas number density $0.1\text{--}5\text{ cm}^{-3}$. At 4 pc resolution the numerical shell radius exceeds the analytic solution by up to 10%, but converges with increased resolution.

When cooling is included the numerical models agree reasonably with the Cioffi *et al.* (1988) offset power law for the shell radial expansion rate, for ambient gas number densities 1 cm^{-3} and below. This is for both cooling functions tested, and notwithstanding the semi-analytic solution applied for a different cooling prescription and was only derived for ambient density 0.1 cm^{-3} . For ambient density 5 cm^{-3} a good agreement with the semi-analytic solution was obtained providing the injection radius was sufficiently small, in this case 3.5 grid cells or 14 pc. Higher density regions require grid resolution better than 4 pc to resolve smaller initial radii, necessary to obtain high enough temperatures to induce a strong enough blast wave. It is worth considering special procedures for handling high density SN sites, depending on the model resolution, such as the momentum injection models proposed by Kim and Ostriker (2015) and Simpson *et al.* (2015), as typically these locations require small injection radii, while for the more diffuse regions, too small a radius can produce too strong a blast wave. Less than 3.5 grid spacing to resolve the initial remnant profile tends to be insufficient to approximate a spherical energy source on the Cartesian domain.

For the ambient density of 1 cm^{-3} the effect of resolution was examined, and convergence to the semi-analytic solution was evident for increases in grid resolution from 4 pc to 0.5 pc, even retaining the same injection radius of 14 pc. For smaller initial radii the convergence with the analytic solution improves further. From grid resolution as good as between 1.0 pc and 0.5 pc the Vishniac-Ostriker-Bertschinger thin shell overstability can be resolved.

To directly induce cooling below the ambient temperature in the remnant shell, as opposed to relying on secondary turbulent effects in shock interactions, a grid resolution of 2 pc or better is required. However, for the purposes of modelling turbulence and the dynamo, where it is adequate to capture the appropriate forcing energy, velocities and length scales to drive the turbulence, even the lowest grid resolution considered here provides good agreement with the analytic solutions. Techniques, such as removing excess mass, may however be required for ensuring regions of density 10 cm^{-3} or higher can be heated sufficiently at the lower resolution.

This detailed analysis of the treatment of strong shocks and minimal diffusivity enables the code to now combine the large scale dynamo processes already present in Gent *et al.* (2013b) with a prescription capable of supporting the small scale turbulent dynamo as present, for example, in Balsara *et al.* (2004). Further, investigation of the dependence and effect of individual SN explosions in idealised uniform and stably stratified ISM with magnetic fields and cosmic rays is a natural extension of the present study.

References

Balsara, D.S., Kim, J., Mac Low, M.M. and Mathews, G.J., Amplification of Interstellar Magnetic Fields by Supernova-driven Turbulence. *ApJ*, 2004, **617**, 339–349.

Brandenburg, A. and Dobler, W., Hydromagnetic turbulence in computer simulations. *Computer Physics Communications*, 2002, **147**, 471–475.

Caunt, S.E. and Korpi, M.J., A 3D MHD model of astrophysical flows: Algorithms, tests and parallelisation. *A&A*, 2001, **369**, 706–728.

Cioffi, D.F., McKee, C.F. and Bertschinger, E., Dynamics of radiative supernova remnants. *ApJ*, 1988, **334**, 252–265.

de Val-Borro, M., Edgar, R.G., Artymowicz, P., Ciecielag, P., Cresswell, P., D’Angelo, G., Delgado-Donate, E.J., Dirksen, G., Fromang, S., Gawryszczak, A., Klahr, H., Kley, W., Lyra, W., Masset, F., Meléma, G., Nelson, R.P., Paardekooper, S.J., Peplinski, A., Pierens, A., Plewa, T., Rice, K., Schäfer, C. and Speith, R., A comparative study of disc-planet interaction. *MNRAS*, 2006, **370**, 529–558.

Dobler, W., Stix, M. and Brandenburg, A., Magnetic Field Generation in Fully Convective Rotating Spheres. *ApJ*, 2006, **638**, 336–347.

Elmegreen, B.G. and Scalo, J., Interstellar Turbulence I: Observations and Processes. *ARA&A*, 2004, **42**, 211–273.

Gent, F.A., Shukurov, A., Fletcher, A., Sarson, G.R. and Mantere, M.J., The supernova-regulated ISM - I. The multiphase structure. *MNRAS*, 2013a, **432**, 1396–1423.

Gent, F.A., Shukurov, A., Sarson, G.R., Fletcher, A. and Mantere, M.J., The supernova-regulated ISM - II. The mean magnetic field. *MNRAS*, 2013b, **430**, L40–L44.

Gent, F.A., Supernova Driven Turbulence in the Interstellar Medium. Ph.D. Thesis, Newcastle University School of Mathematics and Statistics, 2012.

Haugen, N.E.L., Brandenburg, A. and Dobler, W., Simulations of nonhelical hydromagnetic turbulence. *Phys. Rev. E*, 2004a, **70**, 016308.

Haugen, N.E.L., Brandenburg, A. and Mee, A.J., Mach number dependence of the onset of dynamo action. *MNRAS*, 2004b, **353**, 947–952.

Hawley, J.F., Smarr, L.L. and Wilson, J.R., A numerical study of nonspherical black hole accretion. I Equations and test problems. *ApJ*, 1984, **277**, 296–311.

Johansen, A., Klahr, H. and Mee, A.J., Turbulent diffusion in protoplanetary discs: the effect of an imposed magnetic field. *MNRAS*, 2006, **370**, L71–L75.

Johansen, A., Youdin, A. and Klahr, H., Zonal Flows and Long-lived Axisymmetric Pressure Bumps in Magnetorotational Turbulence. *ApJ*, 2009, **697**, 1269–1289.

Joung, M.K.R. and Mac Low, M.M., Turbulent Structure of a Stratified Supernova-driven Interstellar Medium. *ApJ*, 2006, **653**, 1266–1279.

Käpylä, M.J., Gent, F.A., Väistö, M.S. and Sarson, G.R., The supernova-regulated ISM. III. Generation of vorticity, helicity, and mean flows. *A&A*, 2018, **611**, A15.

Käpylä, M.J., Käpylä, P.J., Olspt, N., Brandenburg, A., Warnecke, J., Karak, B.B. and Pelt, J., Multiple dynamo modes as a mechanism for long-term solar activity variations. *A&A*, 2016, **589**, A56.

Käpylä, P.J. and Korpi, M.J., Magnetorotational instability driven dynamos at low magnetic Prandtl numbers. *MNRAS*, 2011, **413**, 901–907.

Käpylä, P.J., Korpi, M.J. and Brandenburg, A., Large-scale dynamos in turbulent convection with shear. *A&A*, 2008, **491**, 353–362.

Käpylä, P.J., Korpi, M.J. and Brandenburg, A., Large-scale Dynamos in Rigidly Rotating Turbulent Convection. *ApJ*, 2009, **697**, 1153–1163.

Käpylä, P.J., Mantere, M.J. and Brandenburg, A., Cyclic Magnetic Activity due to Turbulent Convection in Spherical Wedge Geometry. *ApJ*, 2012, **755**, L22.

Kim, C.G. and Ostriker, E.C., Momentum Injection by Supernovae in the Interstellar Medium. *ApJ*, 2015, **802**, 99.

Mac Low, M.M. and Norman, M.L., Nonlinear growth of dynamical overstabilities in blast waves. *ApJ*, 1993, **407**, 207–218.

McMillan, D.G. and Sarson, G.R., Dynamo simulations in a spherical shell of ideal gas using a high-order cartesian magnetohydrodynamics code. *Physics of the Earth and Planetary Interiors*, 2005, **153**, 124–135.

Mee, A.J.W., Studies of Interstellar Hydromagnetic Turbulence. Ph.D. Thesis, Newcastle University School of Mathematics and Statistics, 2007.

Ostriker, J.P. and McKee, C.F., Astrophysical blastwaves. *RvMP*, 1988, **60**, 1–68.

Raymond, J.C., Cox, D.P. and Smith, B.W., Radiative cooling of a low-density plasma. *ApJ*, 1976, **204**, 290–292.

Rosen, A., Bregman, J.N. and Norman, M.L., Hydrodynamical simulations of star-gas interactions in the interstellar medium with an external gravitational potential. *ApJ*, 1993, **413**, 137–149.

Ryutov, D.D., Cohen, B.I., Cohen, R.H., Hooper, E.B. and Sovinec, C.R., The effect of artificial diffusivity on the flute instability. *Physics of Plasmas*, 2005, **12**, 084504.

Sarazin, C.L. and White, III, R.E., Steady state cooling flow models for normal elliptical galaxies. *ApJ*, 1987, **320**, 32–48.

Scalo, J. and Elmegreen, B.G., Interstellar Turbulence II: Implications and Effects. *ARA&A*, 2004, **42**, 275–316.

Sedov, L.I., *Similarity and Dimensional Methods in Mechanics*, 1959 (New York: Academic Press).

Simpson, C.M., Bryan, G.L., Hummels, C. and Ostriker, J.P., Kinetic Energy from Supernova Feedback in High-resolution Galaxy Simulations. *ApJ*, 2015, **809**, 69.

Sod, G.A., A survey of several finite difference methods for systems of nonlinear hyperbolic conservation laws. *Journal of Computational Physics*, 1978, **27**, 1–31.

Stone, J.M. and Norman, M.L., ZEUS-2D: A radiation magnetohydrodynamics code for astrophysical flows in two space dimensions. I - The hydrodynamic algorithms and tests.. *ApJS*, 1992, **80**, 753–790.

Taylor, G., The Formation of a Blast Wave by a Very Intense Explosion. I. Theoretical Discussion. *Royal Society of London Proceedings Series A*, 1950, **201**, 159–174.

Vishniac, E.T., The dynamic and gravitational instabilities of spherical shocks. *ApJ*, 1983, **274**, 152–167.

Vishniac, E.T., Ostriker, J.P. and Bertschinger, E., Explosions in the early universe. *ApJ*, 1985, **291**, 399–416.

Wolfire, M.G., Hollenbach, D., McKee, C.F., Tielens, A.G.G.M. and Bakes, E.L.O., The neutral atomic phases of the interstellar medium. *ApJ*, 1995, **443**, 152–168.

Woltjer, L., Supernova Remnants. *ARA&A*, 1972, **10**, 129.